PREDICTION OF BVI NOISE RADIATION VARIATION DUE TO HHC USING ADVANCED PRESCRIBED WAKE METHODOLOGY

Berend G. van der Wall
Institute of Flight Systems
berend.vanderwall@dlr.de

Jianping Yin
Institute of Aerodynamics and Flow Technology
jianping.yin@dlr.de

German Aerospace Center (DLR)
Lilienthalplatz 7, 38108 Braunschweig
Germany

Abstract

DLR's comprehensive isolated rotor code S4 is validated with a variety of wind tunnel experimental data from the HART II test of 2001 (Bo105 hingeless Mach-scaled model rotor) at low speed with and without higher harmonic control (HHC) using 3/rev control frequency in descending flight, known to generate strong BVI. To evaluate noise radiation, a coupled S4 and an analytic far field prediction method based on an integral Ffowcs-Williams and Hawkings approach are conducted. Overall, the quality of elasto-mechanical computations, aerodynamic section loads prediction, simulation of the wake geometry and the noise radiation is predicted to a good accuracy, validating the approach of reduced order modeling.

1 INTRODUCTION

Comprehensive codes allow a very fast and efficient computation of a large amount of operational conditions in a short time. This is due to the reduced order modeling of all components, as there are: the blade elasticity, the unsteady section aerodynamics, the wake geometry and the fuselage effect.

Since all interact with each other, it is required to have all of these components at a similarly high level of resolution and consistent with each other in order to be able to simulate the physical effects appropriately and to generate reliable and accurate results. This is especially true when the noise radiation is concerned, that strongly depends on the quality of the wake geometry computation, which in reverse depends both on the blade's unsteady aerodynamic loading and on its motion during the rotor revolution. The high-frequency blade section air loads that cause the blade-vortex interaction (BVI) noise radiation strongly depend on the vortex strength and core radius, the blade-vortex miss-distance and the unsteady lift transfer function during the BVI encounter.

The first item, the vortex strength, depends on the radial gradient of the blade-bound circulation at the time of vortex generation and the vortex aging model. The dynamic blade motion defines both the position of vortex generation and the blade position at the location of BVI, while the wake position at this location is depending on the wake convection from the point of generation until the interaction with a blade takes place. Finally, the aerodynamic response of the blade due to BVI is also depending on the vortex core radius, and the underlying aerodynamics of BVI is an unsteady gust response problem, in contrast to the unsteady aerodynamic problem associated with blade motion. As an example, a very high frequency of airfoil motion causes very high amplitude air loads, while the same frequency of BVI generates air loads with amplitudes approaching zero.

The core radii of blade tip vortices in the rotor wake are the least known parameters to model since only very few measurements exist. Values between 5% and 80% chord have been used, while experimental data indicate that young vortices in hover may be as small as 2% chord, but in forward flight their size also depends on how the vortices are generated, i.e., from a steep gradient of blade circulation or during a roll-up process of weak wake vorticity distributed over a long radial extension of the outer blade.

2 EXPERIMENTAL DATA

To support the comprehensive code physical modeling and validation, a number of wind tunnel experiments have been performed in the past that cover measurements of all aspects mentioned, i.e.:

- Rotor operational conditions
- Hub forces, moments and controls (trim)
- Blade motion in flap, lag, torsion
- Unsteady air loads at several stations along span
- Noise radiation below the rotor
- Wake geometry (position)
- Vortex parameters (circulation, core radius, swirl)

The HART I test of 1994 had a wide range of test conditions covering advance ratios of μ = 0.114, 0.151 and 0.275 – all with 3, 4 and 5/rev HHC applied[1],[2]. However, wake measurements were missing, which led to the HART II test in 2001.

In this paper, data are taken from the HART II experiment[3],[4],[5], where at an advance ratio of μ = 0.151 a shaft angle variation was performed to identify the setting for maximum noise radiation, and therein a 3/rev higher harmonic control with a phase variation for BVI noise radiation studies was applied. DLR's Bo105 Mach and dynamically scaled hingeless 4-bladed model rotor with rectangular blades, NACA 23012 airfoil with a trailing edge tab, -8° pre-twist, radius R = 2 m, chord c = 0.121 m was used in HART I and HART II.

This rotor was also used in the HELINOISE test 1992[6],[7], where a very high speed condition without HHC is available with an advance ratio of μ = 0.36. Deep dynamic stall and related blade torsion investigations have been made at Onera with an articulated Mach-scaled 7AD model rotor, operated at reduced RPM to obtain an advance ratio of μ = 0.4 at very high rotor loading[8],[9]. Due to size limitations of the paper, only the HART II data are used here for validation purposes and the validation with the other test data is left for future publications.

3 ROTOR SIMULATION CODE

DLR's high resolution 4th generation rotor simulation code (S4) has its origins in the mid-'70s with rigid flapping, constant downwash, and steady table look-up of aerodynamic coefficients. The development goal to simulate HHC for an isolated rotor required elastic blade modeling in flap, lag, and torsion, unsteady aerodynamics, and a downwash model including higher harmonic contributions. Later BVI noise radiation became important, thus a vortex wake model was added. Today, S4 can be used for any kind of active rotor control with respect to performance, dynamics, and noise and to support wind tunnel testing[10].

3.1 Structural mechanics

The structural dynamics modeling consists of two parts. First, a finite element method (FEM)[11] based on the Houbold-Brooks formulation[12] is used for the modal analysis, i.e., it computes the coupled mode shapes and natural frequencies *in vacuo*. The beam elements used have ten degrees of freedom (deflection and gradient at both ends for flap and lag; twist angle at both ends for torsion). Only the major component of the mode shapes is then represented analytically as a 7th order polynomial in the radial coordinate direction. All mass integrals required in the differential equations of motion, as well as for computation of the blade root forces and moments, are evaluated in post-processing. This includes mechanical couplings like flap-torsion coupling caused by an offset of the mass axis from the elastic axis. Thus, the structural discretization used for modal analysis is completely independent of the aerodynamic discretization used in rotor simulation.

In a second step which is independent of the FEM, the rotor simulation itself solves the dynamic response problem of these modes (which are reduced to their major component) subjected to the aerodynamic loading in the form of a modal synthesis. In the computations shown in this paper, four flap modes, two lag modes, and two torsion modes have been retained, which cover the frequency range up to 10/rev. A higher number of modes has also been examined, but the mode deflections were found to be so small that they do not contribute to the results and thus were omitted.

The bending moments are computed using the modal method. At the radial location of the moment of interest the local value of blade bending stiffness is multiplied with the second derivative of the respective mode at this station (computed analytically from the polynomial representation) and with the associated generalized deflection. All individual modes' contributions are added.

3.2 Section aerodynamics

For two-dimensional unsteady compressible section air loads, a semi-empirical analytic formulation of the airfoil coefficients $C_n M^2$, $C_m M^2$ and $C_t M^2$ is used within S4, originally based on the formulation of Leiss[13] but significantly enhanced today. The fundamental functionality is that the effective instantaneous angle of attack as well as the effective instantaneous stall angle of attack are differential equations of motion using arbitrary motion theory. The instantaneous stall angle of attack modifies the instantaneous curves of lift, drag, and moment, while the effective instantaneous angle of attack defines the instantaneous working position on this curve. Together with the non-circulatory air loads, this provides smooth loops in attached flow (representing Theodorsen incompressible flow theory[14]) and dynamic stall hysteresis when flow separation occurs. The parameters of the functions computing lift, drag, and moment are identified from the steady measured polars or from those computed by CFD. The effects of leading or trailing edge flap deflections are also included. Once the steady model is identified, the parameters of the unsteady model are assumed to be valid for all airfoils since the shape of the unsteady hysteresis is assumed to be dominated by the steady airfoil characteristics.

A distinction between unsteady aerodynamics due to body motion (causing a constant or linear variation of velocities along the airfoil chord) and due to gusts (as caused by a vortex with strong non-linearity along the chord) is made. The formulation of arbitrary motion is chosen in both cases, thus at an airfoil section only one observer location is needed to compute the normal velocities of these two separately. Next, the respective unsteady transfer function of step inputs is applied (Wagner function[15] for

the airfoil motion and Küssner function[16] for the gust, both with compressibility corrections), and the effective angle of attack is computed using the Duhamel integral formulation[17].

High-frequency vortex shedding during the separated flow phase is added. The tip loss of lift is accounted for in the outer 5% of the blade by modifying the induced velocities progressively towards the tip such that the zero lift angle of attack is obtained there. Also, fuselage interference flow is computed at the blade sections by an analytical formulation, derived from potential theory calculations[18]. Validations of the model for dynamic stall including yaw, active trailing edge flaps, and for the BVI problem were performed[8],[9],[19],[20].

3.3 Rotor wake

Initially, the Mangler and Squire[21] global wake model was included, which was acceptable for the dynamics problems, as it provided higher harmonic downwash components. However, these were only dependent on the steady rotor operational condition and thus any variation of blade harmonic loading - either due to the aerodynamic environment like high-speed or due to active control of the blade - was not causing any modifications of induced velocities. Therefore, to address the needs of noise radiation prediction, Beddoes' prescribed wake geometry formulation[22] was added, but keeping the full vortex spiral in contrast to Beddoes' suggestion to replace every loop by a pair of straight line vortices. A multiple trailer enhancement was made to account for the root, tip, and inboard vortices in the far wake. The near wake covering the first 45° behind the trailing edge of a blade is fully occupied with trailers to the right and left of every aerodynamic segment. The far wake starts where the near wake ends and is truncated after five revolutions. The shed far wake is ignored since it usually is one order of magnitude less than the trailed wake, and the near shed wake is inherently included in the unsteady aerodynamic formulation.

The vortex strength of the tip vortex is the maximum circulation of the outer part of the blade. In case it is negative due to download at the tip, the inboard vortex is fed with the difference of maximum positive and maximum negative circulation found in the outer half of the blade. The root vortex strength is the same as the tip vortex (in case of only one tip vortex) or the same as the inboard vortex (when dual vortex systems are present).

Since the geometry of the wake is tied to the operational condition, the only geometric modification of the wake during HHC is a result of the different blade motion. To account for the additional (and dominant) wake deflections due to harmonic blade loading and its associated upwash and downwash, an upgrade in the form of additional perturbations to the prescribed wake geometry was derived using a momentum theory approach[23]. The fuselage interference with the wake geometry is discussed therein as well, but currently is has not yet been included.

A free-wake to run on massive parallel computers was also developed at DLR for a loose coupling with the S4 code[24]. It has a full wake with trailers at the radial boundaries of all aerodynamic blade sections and shed vortex elements, spatially discretized in 5° segments. The time integration of the wake geometry was performed in 1° azimuth steps, and special care was given to close encounters of a wake node to any of the wake vortices, including local refinement. However, the availability of massive parallel computers for short periods (less than 15 minutes for a converged solution on about 100 processors) was not efficient and the waiting time nullified the overall performance. In addition, the upgrades of the prescribed wake performed well such that its usage is standard today, and all DLR results of this paper are obtained with it.

3.4 Trim computation

Trim to the experimental thrust and hub moments is performed using time integration by means of a fourth-order Runge-Kutta scheme with azimuthal increments of 1° (intermediate step at every 0.5°). The radial discretization of the airfoil portion of the blade features 40 elements, non-equidistantly distributed with higher density at the blade tip such that every blade element covers the same ring surface of the rotor disk. The trim algorithm iteratively computes the derivatives of thrust and moments with respect to the control angles and based on these, the corrective angles for the next trim step are evaluated. The wake geometry is updated once a trim cycle with associated blade motion and air loads is finished and the influence coefficients of the new wake geometry are updated before the next trim cycle starts. During the trim, the induced velocities of the far wake are updated every few revolutions to account for the variations of changing air loads and modified vortex strengths as a consequence of these.

3.5 Noise radiation

Based on the operational condition, the blade motion and the blade loading in terms of the section normal force provided from the S4 code, the noise radiation on a prescribed plane in space is computed using the acoustic code APSIM from the DLR Institute of Aerodynamics and Flow Technology[25]. The methodology of APSIM is based on both permeable and non-permeable Ffowcs-Williams and Hawkings formulation[26] as well as Kirchhoff formulations[27]. Only linear sound propagation is taken into account when sound propagating away from the noise source sur-

face is computed. The acoustic results presented here are the sum of thickness noise and loading noise, the latter responsible for BVI noise radiation which is of interest here. The quadruple noise contributions are not considered and assumed to be negligible for the flight conditions used in the paper. As S4 can only provide unsteady lifting line air loads, the Ffowcs-Williams and Hawkings formulation based on lifting line air loads is used[28]. The calculations, performed in the time domain, deliver a pressure time history at any observer location. This sound pressure time history is transformed into a Fourier series to obtain the acoustic spectrum. The code validation of all these aspects including rotor BVI noise radiation was presented in 2003[28].

4 RESULTS

The operating condition is a trim to a rotor loading of C_T/σ = 0.0057 at an advance ratio of μ = 0.151 with zero hub roll and pitch moments. A shaft angle variation was performed in the experiment first to identify the setting for maximum noise radiation. Then a 3/rev HHC blade root pitch angle of 0.8° amplitude was applied (while re-trimming) and its phase varied to identify its impact on blade motion, noise radiation and vibration. The shaft angles given here are corrected for wind tunnel interference and represent free-flight settings.

4.1 Shaft angle variation

Trim results for rotor controls in collective Θ_0, longitudinal cyclic Θ_{1S} and lateral cyclic Θ_{1C} and power consumed P are given in Figure 1 for a variation of the shaft angle α_S. The absolute values of cyclic controls are predicted to an accuracy of less than 0.3° while the collective is consistently 0.7° below the experiment, indicating less steady torsion in simulation. The power is in excellent agreement with the experiment.

Figure 2 compares the elastic blade tip motion in terms of torsion Θ_{el} and elastic blade flap deflection z_{el}/R to experimental data. The mean torsion is less in simulation, partially explaining the lower collective. Essentially a 2/rev torsion is present in the experiment, which is predicted in phase, but not as much in magnitude. The flapping motion is predicted well in the mean value and in the fundamental characteristics of its dynamic content. The 1/rev part in the experiment is larger than in the simulation, which indicates that a larger rolling moment was apparent than that prescribed in the trim of the simulation. It is equivalent to 0.2° lateral cyclic control in Θ_C, or about 50 Nm rolling moment, which is a small amount for this rotor.

The section loading in terms of the normal force coefficient C_nM^2 at 0.87R is compared in Figure 3. The fundamental change of the normal force coefficient with shaft angle variation is captured in trend quite well, although not in all details. However, the appearance of high-frequency BVI loading and its azimuthal position, as well as its magnitude, is captured sufficiently well. Especially the shaft angle setting of α_S = +4.5° appears to be generating the highest noise radiation. More details are visible in Figure 4, where the 10/rev high-pass filtered section loading is shown for the entire rotor disk, which gives the best indication of BVI locations and intensity. While the experiment had only leading edge pressure sensors over a wide radial extent the simulation can only provide section loading due to the lifting line approach. Therefore, the comparison of these data can only be qualitative.

For most of the shaft angles the predicted locations of BVI are quite similar to the experiment, especially for those conditions of high noise radiation where BVI is present in the first and fourth quadrant of the disk, i.e. within the azimuth ranges Ψ = 0° – 90° and 270° - 360°. For the smallest and largest shaft angles (Figure 4 (a) and (i)) the experiment still shows some BVI but the simulation predicts the blade tip vortices obviously farer away from the disk in these cases (below the disk in (d) and above it in (l)) with significantly reduced BVI intensity. Finally, the noise radiation of these cases is shown in Figure 5. These results are in agreement with the observations just made. For the smallest and largest shaft angles the prediction is 6-8 dB less than the experiment, but the overall levels are low compared to the high BVI conditions. The shaft angle of maximum noise radiation is found the same in experiment and simulation. The difference in noise levels between both at this shaft angle is 2 dB only. In general, for the variation of shaft angles the changes of directivity and intensity are captured quite well in trend by the simulation.

4.2 3/rev HHC phase sweep

At the shaft setting of maximum noise radiation, α_S = +4.5°, a 3/rev HHC blade root pitch control angle of Θ_3 = 0.8° was introduced and its phase varied from Ψ_3 = 0° to 360° in increments of 30°. Here, the results are compared in steps of 60° due to limited space. Such high-frequency input will generate larger dynamic blade response in elastic flapping and in torsion, and blade-to-blade differences in the experiment will become more apparent, while the simulation assumes identical blades and blade properties were adjusted to the reference blade 1. Figure 6 gives an impression of the blade-to-blade differences in flap and torsion, compared to the mean of all four blades. It is obvious that the blade 1 has always a larger dynamic content than all others, which is due to the retrofit of this blade with pressure sensors while the other blades were unchanged. The mean therefore has smaller amplitudes than blade 1. This should be kept in mind since in the

following the experiment is represented by the mean of all four blades, and the differences of blade 1 to the mean can be up to 0.01R in flap and more than 1° in torsion.

A 3/rev HHC will have some impact on the 0/rev and 1/rev loading of the rotor and thus on the rotor trim. In the experiment as well as in simulation the rotor was re-trimmed and the variation of rotor controls and power is given in Figure 7. The variation of controls with the HHC phase is small and more pronounced as a sinusoidal variation in the simulation than the experiment suggests, but the overall agreement is very good and the differences are of the same order as observed during the shaft angle variation. Larger variations are predicted by simulation in rotor power, although the trend of power variation is visible in the experiment as well. However, the maximum difference is 4kW, which is a small value since the mean of about 20kW is a low power for this rotor, but characteristic for this descending flight condition.

The blade motion for the HHC phase sweep is shown in Figure 8 for the baseline case (BL) without HHC and two phase settings of Ψ_3 = 180° (called minimum vibration setting, MV) and 300° (minimum noise, MN). The blade motion has been measured only at these two HHC settings. The dynamics of blade motion relative to the BL case, and the variation with HHC phase, are well predicted by simulation while the magnitude of the dynamics appears quite larger than the experiment. However, the experimental data are the mean of all four blades with blade 1 always having larger deflections as explained before. It is important to predict the correct phasing of blade motion.

Section airloads at 0.87R are shown in Figure 9 for the full set of HHC phase variations. Due to 3/rev HHC this frequency is well visible in the data with correct phase predicted, but the magnitude over-predicted, in accordance with the larger blade torsion shown before. A variation of BVI location and intensity especially on the advancing side is seen both in experiment and prediction, while on the retreating side the variations are minor in both. A better judgment of the BVI locations is possible with the contours of the high-frequency part of the loading in the rotor disk, shown in Figure 10. At Ψ_3 = 0° the advancing side BVI is quite intense and at an azimuth of about 70°. With increasing HHC phase this interaction moves downstream towards an azimuth of about 30° while simultaneously getting less intense. On the retreating side a similar but less pronounced behavior is seen: the BVI move from 290° azimuth to 310° for the same HHC phase variation. Both of these effects are predicted quite well by simulation, indicating that the principal effects of HHC on the wake geometry are captured.

When further varying the HHC phase from Ψ_3 = 180° to 300° the advancing side BVI are getting stronger and move progressively inboard, leaving the blade tip region almost free of BVI at the 300° setting. On the retreating side the BVI locations move upstream and intensify. Again, both these effects are represented by simulation quite well. A more quantitative judgment of the simulation results can be made by the noise radiation given in Figure 11. For the BL case, the simulation predicted sufficiently well the experimental noise carpet in both noise level and directivity. The relative variation of both of these parameters with 3/rev HHC phase is the most challenging part of the simulation.

For the variation of Ψ_3 from 0° to 120° the advancing side BVI “hot spot” moves from a position centered below the second quadrant towards the right side with simultaneous reduction of intensity – an effect predicted in trend as well by the simulation, although larger than the experiment. In the further phase variation the advancing side “hot spot” is moving forward again, being most intense at 180° and 240°, and reaching the most forward-oriented and less intense position for 300° phase. Again, the simulation does predict this behavior quite well in trend.

Finally, the wake trajectories from experiment and simulation are compared. The wake is the key to BVI noise prediction and its position must be correctly predicted in order to get physically relevant results. Measurements were performed at various lateral positions. The 70% lateral position is considered most important and representative for BVI investigations. Figure 12 compares the advancing side trajectories of the BL and MN cases in (a) and in (b) the MV case, where due to blade tip download a dual vortex system is generated with a vortex of opposite sense of rotation right at the tip (counter-rotating vortex = cv) and one representative for lifting blades, which is released much more inboard of the blade.

First, the major effect of the MN HHC setting is a much stronger downward convection of the tip vortex relative to the BL case. This leads to a larger blade-vortex separation in the MN case and consequently reduces the advancing side noise radiation. The penetration through the rotor disk happens at a more upstream position as already seen in Figure 10. This trend is captured quite well in simulation. The strong curvature of the measured vortex trajectory indicates a large induced inflow gradient in downstream direction, which is under-predicted in simulation.

Figure 12 (b) compares the dual vortex trajectories of the MV case with the experiment. The agreement is surprisingly good for both of the vortices. The inboard vortex position could not be identified for more upstream positions since this vortex was not yet rolled up there. The retreating side trajectories

reveal only a tip vortex and results are shown in (c). It was already apparent from the section loading in Figure 9 that the retreating side BVI did not change much during HHC phase variations, which is clearly seen in this figure and also predicted this way. The absolute positions are not matched, but the relative change of the trajectory depending on HHC phase is matched very well.

With respect to wake geometry predictions it must be recalled that the Beddoes' prescribed wake fundamental geometry is based on a global inflow model (here that one of Drees[30]) that predicts a longitudinal gradient of the order of $k_x = (1/\lambda_0)*(d\lambda/dx) = 1.25$, where λ_0 is the mean induced inflow. The vortex trajectory is the integral over all induced velocities encountered along x, thus a linear gradient of these velocities causes a parabolic trajectory. The gradient is larger than 1, therefore in the front of the rotor disk an upwash is present, initially convecting the tip vortex upwards until the sign changes from up- to downwash and the vortex will progressively convect downwards. This inflow gradient is analyzed from the induced velocity distribution resulting from the entire prescribed wake system during the simulation and Drees' model is then updated iteratively for the gradients identified.

Figure 13 shows the downstream and lateral inflow gradients k_x and k_y predicted by the Drees model for this operating condition and the gradients identified from the induced velocity distribution computed by the prescribed wake. Almost twice the value in downstream direction is found for the entire shaft angle variation, while the HHC phase variation at constant shaft angle also has a large impact on this gradient. The lateral gradient is much smaller, and the analysis of the computed induced velocity field predicts much smaller values than the Drees model. The variation of the lateral gradient due to HHC is also small compared to the impact on the downstream gradient. A comparison of induced inflow gradients derived from the experiment with eight different models of various authors revealed values of k_x ranging from 0.98 to 2.9, while the experiment resulted in 3.6 – much more than any of the models predicts[31]. Therefore, the iterative identification of this gradient from the induced velocity field computed by the prescribed wake system appears to be a very suitable solution to adapt the prescribed wake geometry model to the individual operational situation.

5 CONCLUSIONS

For a range of shaft angles and a 3/rev HHC phase variation the blade motion, section loading, BVI locations, noise radiation and wake trajectories have been compared for experimental data from HART II and the comprehensive rotor simulation code S4 of DLR. It is found that in all aspects the general behavior is predicted sufficiently well. This is especially noteworthy since a prescribed wake is used throughout instead of a free-wake, because of the gain in computational efficiency. The quality of the results is only possible due to the introduction of fundamental physical effects into the prescribed wake geometry, such as the adaptation of the longitudinal and lateral gradients of the induced inflow field and the superposition of a higher harmonic induced inflow field caused by the dynamic part of the blade loading. The results obtained validate this approach. In the future, the fuselage induced velocity effect on the wake geometry will also be investigated and routinely included in rotor simulations.

REFERENCES

[1] Y.H. Yu, C. Tung, J. Gallman, K.-J. Schultz, B.G. van der Wall, P. Spiegel, B. Michea: Aerodynamics and Acoustics of Rotor Blade-Vortex Interactions, Journal of Aircraft, **32** (5), 970-977, 1995

[2] W.R. Splettstößer, R. Kube, U. Seelhorst, W. Wagner, A. Boutier, K. Pengel: Higher Harmonic Control Aeroacoustic Rotor Test (HART) – Test Documentation and Representative Results –, DLR IB 129-95/28, Braunschweig, 1995

[3] B.G. van der Wall, C.L. Burley, Y. Yu, K. Pengel, P. Beaumier: The HART II Test – Measurement of Helicopter Rotor Wakes, Aerospace Science and Technology, **8** (4), 273-284, 2004

[4] B.G. van der Wall: 2nd HHC Aeroacoustic Rotor Test (HART II) – Part I: Test Documentation –, DLR IB 111-2003/31, Braunschweig, 2003

[5] B.G. van der Wall, C.L. Burley: 2nd HHC Aeroacoustic Rotor Test (HART II) – Part II: Representative Results –, DLR IB 111-2005/03, Braunschweig, 2005

[6] W.R. Splettstößer, G. Niesl, F. Cedenese, F. Nitti, D.G. Papanikas: Experimental Results of the European HELINOISE Aeroacoustic Rotor Test, Journal of the American Helicopter Society, **40** (2), 3-14, 1995

[7] W.R. Splettstößer, B. Junker, K.-J. Schultz, W. Wagner, W. Weitemeyer, A. Protopsaltis, D. Fertis: The HELINOISE Aeroacoustic Rotor Test in the DNW – Test Documentation and Representative Results –, DLR-Mitteilung 93-09, Braunschweig, 1993

[8] D. Petot, G. Arnaud, R. Harrison, J. Stevens, D. Teves, B.G. van der Wall, C. Young, E. Széchényi: Stall Effects and Blade Torsion - An Evaluation of Predictive Tools, 23rd European Rotorcraft Forum, Dresden, Germany, 1997

[9] D. Petot, G. Arnaud, R. Harrison, J. Stevens, D. Teves, B.G. van der Wall, C. Young, E. Szé-

chényi: The Prediction of Dynamic Stall and Blade Torsion, (final report of HC/AG-10), GARTEUR TP 114, 1998

[10] B.G. van der Wall: Analytic Formulation of Unsteady Profile Aerodynamics and its Application to Simulation of Rotors, ESA-TT-1244, 1992 (Translation of DLR-FB 90-28, 1990)

[11] W. von Grünhagen: Bestimmung der gekoppelten Schlagbiege-, Schwenkbiege- und Torsionsschwingungen für beliebige Rotorblätter mit Hilfe der Finite-Element-Methode (Computation of the coupled flap bending, lag bending and torsion oscillations for arbitrary rotor blades with the aid of the finite element method), DFVLR IB 154-80/21, Braunschweig, 1980

[12] J.C. Houbold, G.W. Brooks: Differential Equations of Motion for Combined Flapwise Bending, Chordwise Bending, and Torsion of Twisted Nonuniform Rotor Blades, NACA TN 3905, 1957

[13] U. Leiss: A Consistent Mathematical Model to Simulate Steady and Unsteady Rotor-Blade Aerodynamics, 10th European Rotorcraft Forum, The Hague, Netherlands, 1984

[14] T. Theodorsen: General Theory of Aerodynamic Instability and the Mechanism of Flutter, NACA TR 496, 1934

[15] H. Wagner: Über die Entstehung des dynamischen Auftriebes von Tragflügeln, (About the Development of Dynamic Lift of Wings), Zeitschrift für Angewandte Mathematik und Mechanik, **5** (1), 17-35, 1925

[16] H.G. Küssner: Zusammenfassender Bericht über den instationären Auftrieb von Flügeln, (Summary Report about the Unsteady Lift of Wings), Luftfahrt-Forschung, **13** (12), 410-424, 1936

[17] R.L. Bisplinghoff, H. Ashley, R.L. Halfman: Aeroelasticity, Addison-Wesley Publ. Comp. Inc., Reading, MA, USA, 1957

[18] B.G. van der Wall, C. Göpel: Über den Einfluss der Rotorversuchsstände ROTEST und ROTOS auf die Rotordurchströmung im DNW, (About the Influence of the Rotor Test Rigs ROTEST and ROTOS on the Flow in the Rotor Disk in DNW), DLR-Mitteilung 91-16, 1991

[19] B.G. van der Wall, W, Geißler: Experimental and Numerical Investigations on Steady and Unsteady Behaviour of a Rotor Airfoil with a Piezoelectric Trailing Edge Flap, 55th Annual Forum of the American Helicopter Society, Montreal, Canada, 1999

[20] B.G. van der Wall, J., Yin: DLR's S4 Rotor Code Validation With HART II Data: The Baseline Case, 1st International Forum on Rotorcraft Multidisciplinary Technology, Seoul, Korea, 2007

[21] K.W. Mangler, H.B. Squire: The Induced Velocity Field of a Rotor, ARC R&M 2642, 1950

[22] T.S. Beddoes: A Wake Model for High Resolution Airloads, AHS/ARO 1st International Conference on Rotorcraft Basic Research, Research Triangle Park, NC, USA, 1985

[23] B.G. van der Wall: Extensions of prescribed wake modeling for helicopter rotor BVI noise investigations, CEAS Aeronautical Journal, **3** (1), 93-115, 2012

[24] B.G. van der Wall, M. Roth: Free-Wake Analysis on Massively Parallel Computers and Validation with HART Test Data, 53rd Annual Forum of the American Helicopter Society, Virginia Beach, VA, USA, 1997

[25] J. Yin, S. Ahmed: Aerodynamics and Aeroacoustics of Helicopter Main-Rotor/Tail-Rotor Interaction, 5th AIAA/CEAS Aeroacoustics Conference and Exhibit, Bellevue, WA, USA, 1999

[26] J.E. Ffowcs-Williams, D.L. Hawkings: Sound Generation by Turbulence and Surfaces in Arbitrary Motion, Philosophical Transactions of the Royal Society, A264, 1969

[27] K.S. Brentner, F. Farassat: Analytical Comparison of the Acoustic Analogy and Kirchhoff Formulation for Moving Surfaces, AIAA Journal, **36** (8), 1379-1386, 1998

[28] J. Yin, J. Delfs: Improvement of DLR Rotor Aero-acoustic Code (APSIM) and its Validation with Analytic Solution, 29th European Rotorcraft Forum, Friedrichshafen, Germany, 2003

[29] B.G. van der Wall, J.W. Lim, M. Smith, S.N. Jung, J. Bailly, M. Amiraux, D.D. Boyd: An Assessment of Comprehensive Code Prediction State-of-the-Art Using the HART II International Workshop Data, 68th Annual Forum of the American Helicopter Society, Fort Worth, TX, USA, 2012

[30] J. Meijer-Drees: A Theory of Airflow Through Rotors and its Application to Some Helicopter Problems, Journal of the Helicopter Association of Great Britain, **3** (2), 79-104, 1949

[31] B.G. van der Wall, J. Yin: Simulation of Active Rotor Control by Comprehensive Rotor Code with Prescribed Wake using HART II Data, 65th Annual Forum of the American Helicopter Society, Grapevine, TX, USA, 2009

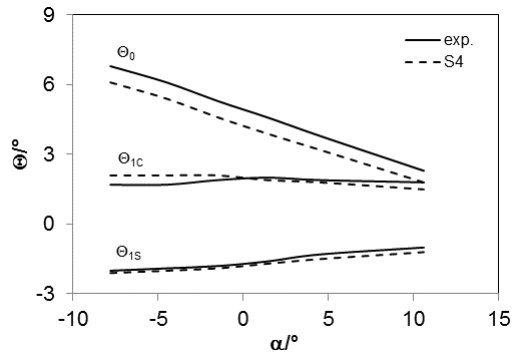

(a) controls

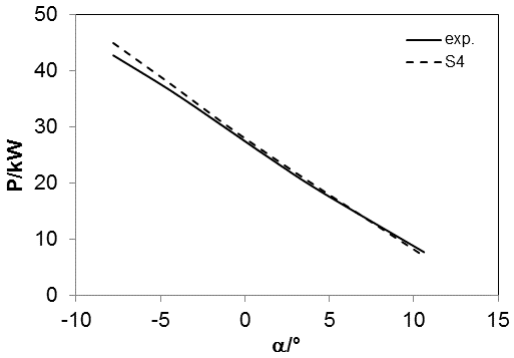

(b) power

Figure 1: Shaft angle sweep; rotor trim

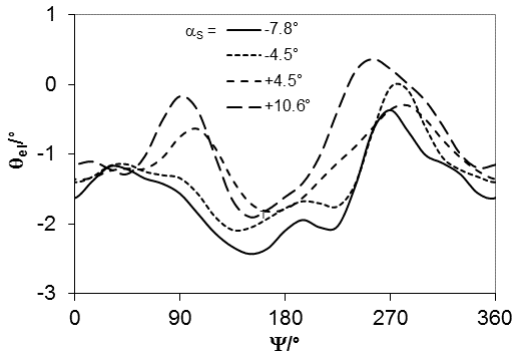

(a) torsion, exp.

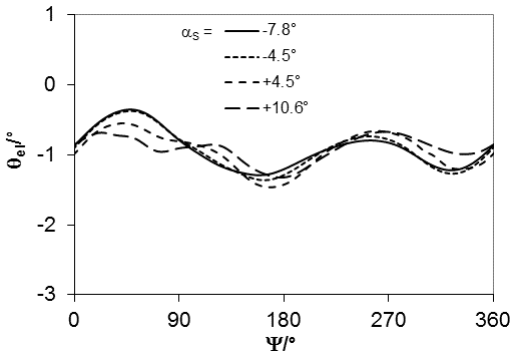

(b) torsion, S4

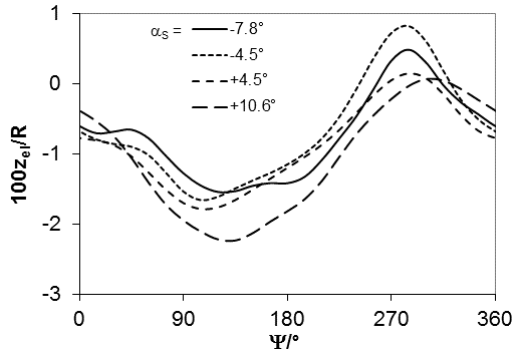

(c) elastic flapping, exp.

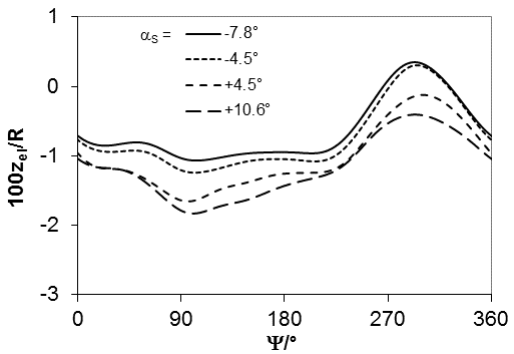

(d) elastic flapping, S4

Figure 2: Shaft angle sweep; blade tip motion

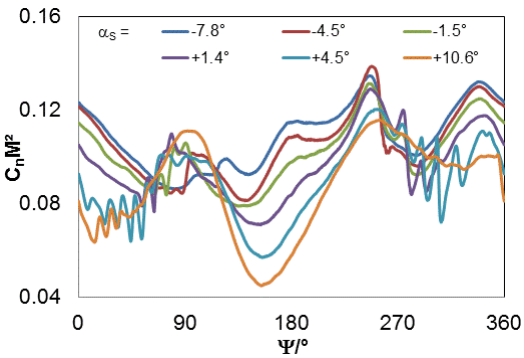

(a) exp.

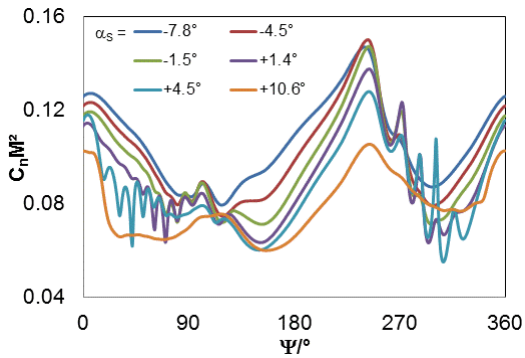

(b) S4

Figure 3: Shaft angle sweep; section loading at 0.87R

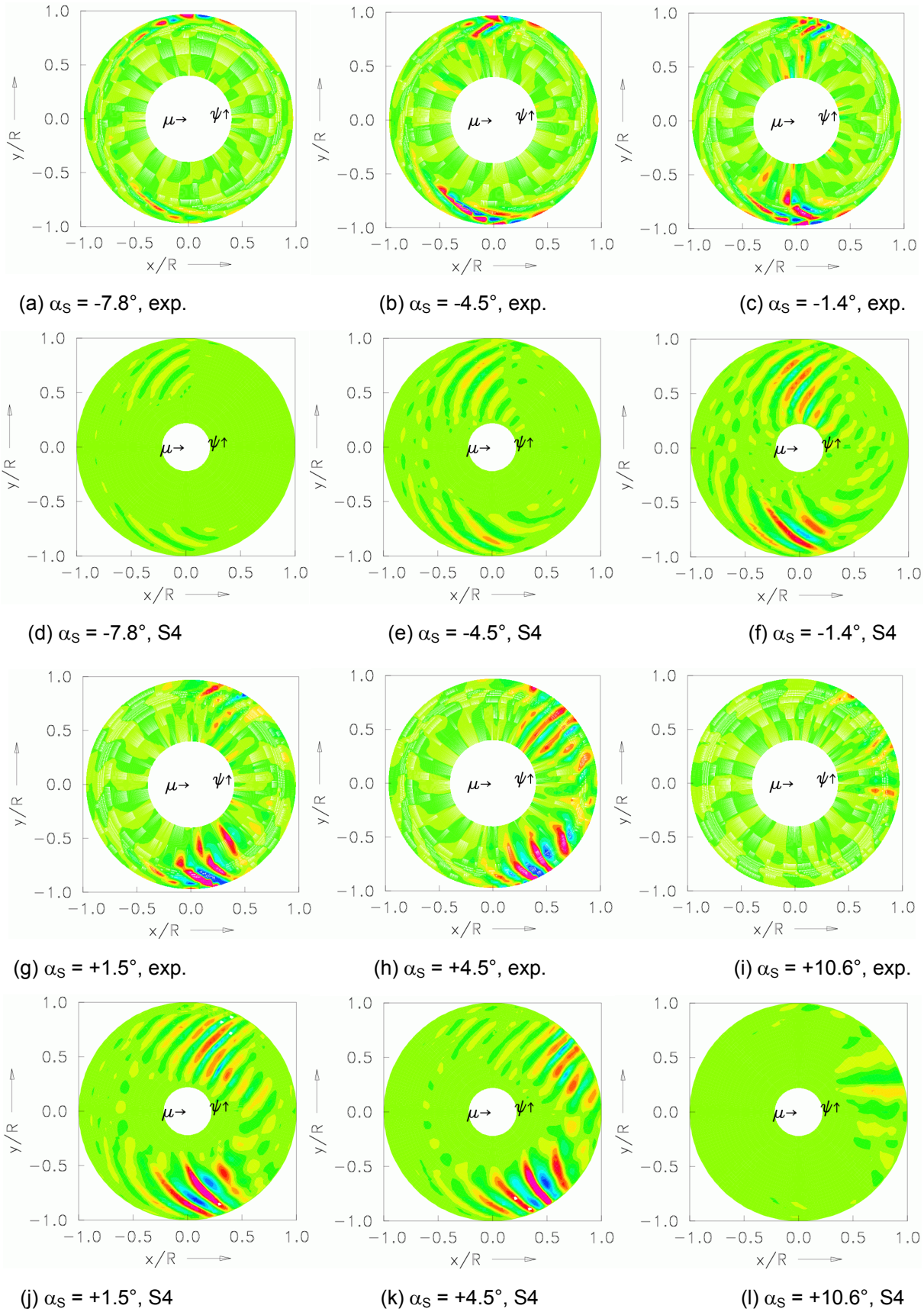

(a) α_S = -7.8°, exp. (b) α_S = -4.5°, exp. (c) α_S = -1.4°, exp.

(d) α_S = -7.8°, S4 (e) α_S = -4.5°, S4 (f) α_S = -1.4°, S4

(g) α_S = +1.5°, exp. (h) α_S = +4.5°, exp. (i) α_S = +10.6°, exp.

(j) α_S = +1.5°, S4 (k) α_S = +4.5°, S4 (l) α_S = +10.6°, S4

Colors represent 10/rev high-pass filtered contours of $\Delta C_P M^2$ (exp.) and $C_n M^2$ (S4)

Figure 4: Shaft angle sweep; BVI locations

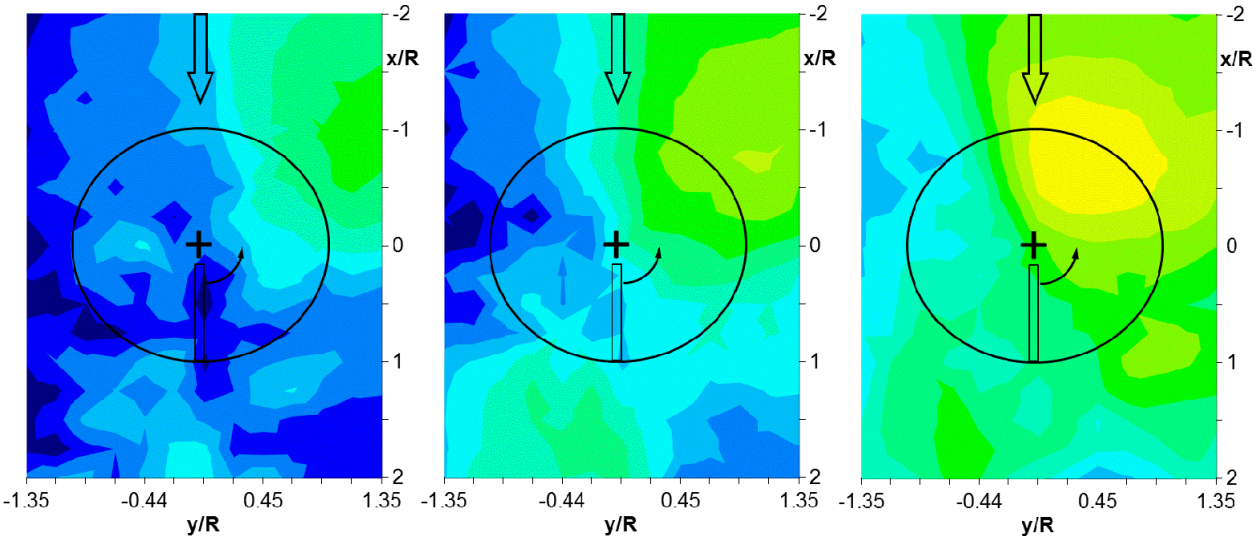

(a) α_S = -7.8°, exp. (b) α_S = -4.5°, exp. (c) α_S = -1.5°, exp.

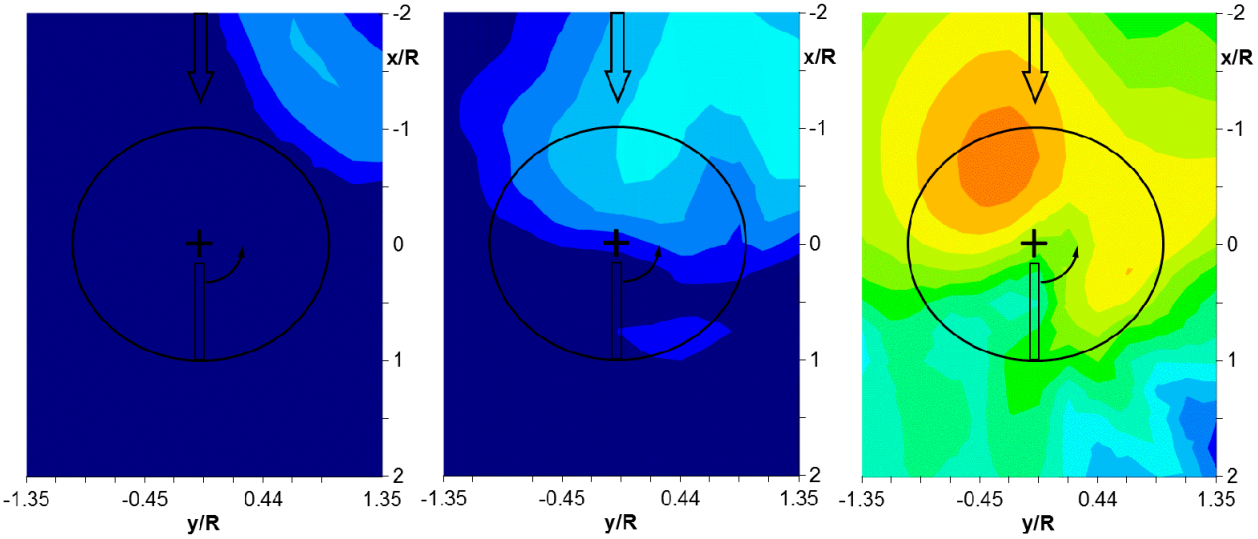

(d) α_S = -7.8°, S4 (e) α_S = -4.5°, S4 (f) α_S = -1.5°, S4

Color scale: mid-frequency noise level (6-40 bpf) from 74 dB (dark blue) to 114 dB (dark violet)

Figure 5: Shaft angle sweep; noise radiation (first part)

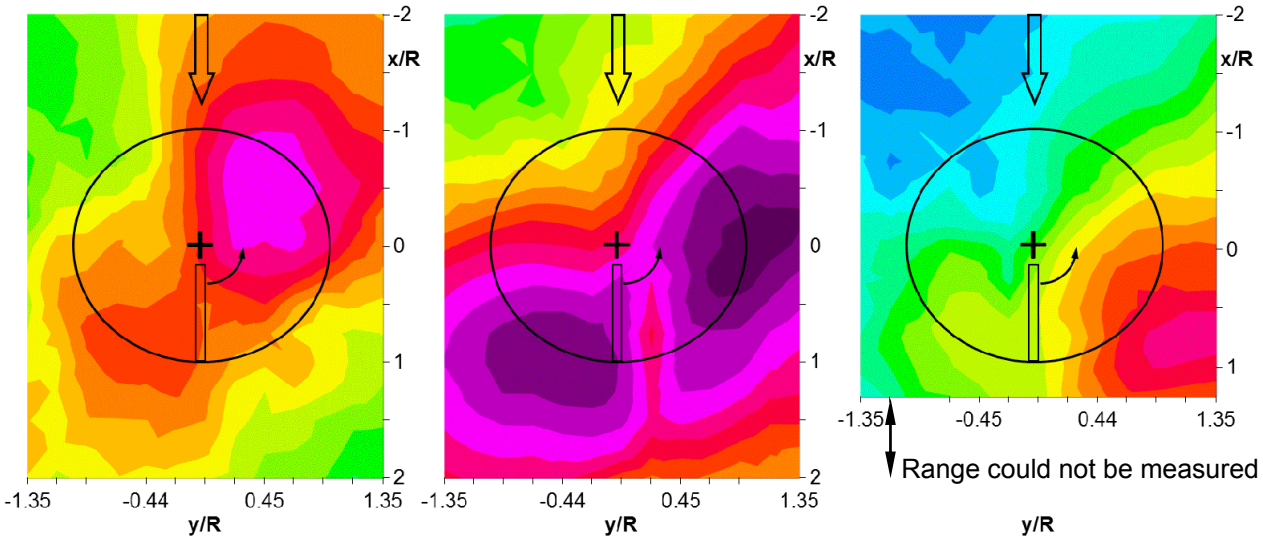

(g) α_S = +1.4°, exp. (h) α_S = +4.5°, exp. (i) α_S = +10.6°, exp.

(j) α_S = +1.4°, S4 (k) α_S = +4.5°, S4 (l) α_S = +10.6°, S4

Color scale: mid-frequency noise level (6-40 bpf) from 74 dB (dark blue) to 114 dB (dark violet)

Figure 5: Shaft angle sweep; noise radiation (second part)

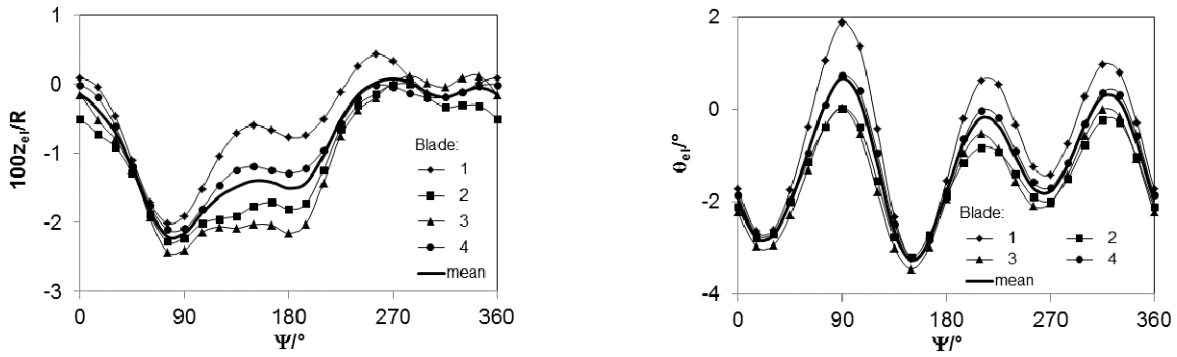

(a) elastic flapping (b) torsion

Figure 6: α_S = +4.5°, 3/rev HHC for minimum vibration; blade motion scatter, exp.

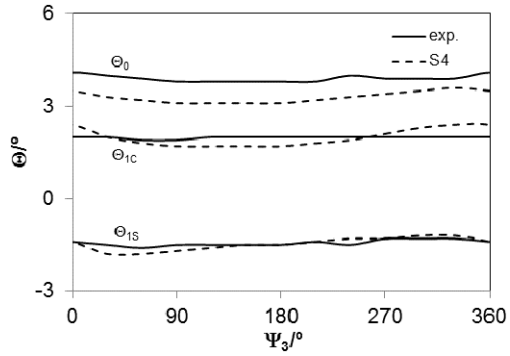

(a) controls

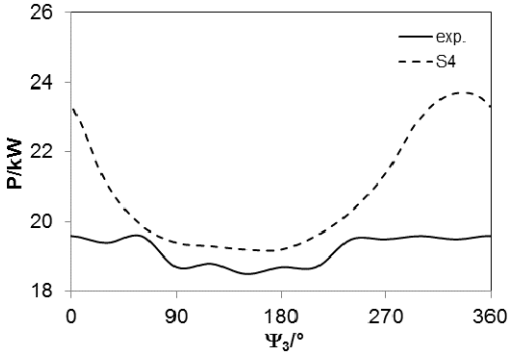

(b) power

Figure 7: α_S = +4.5°, 3/rev HHC phase sweep; rotor trim

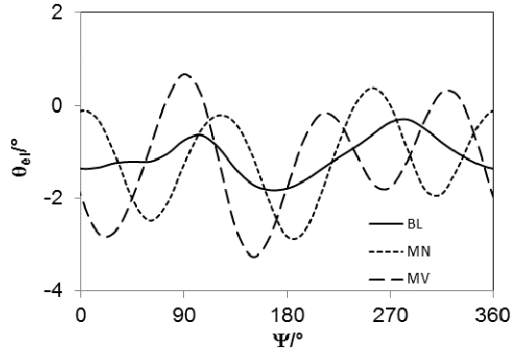

(a) torsion, exp.

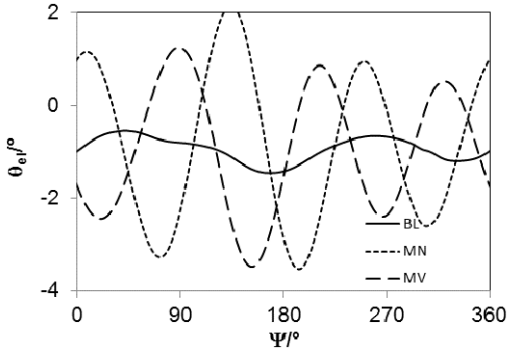

(b) torsion, S4

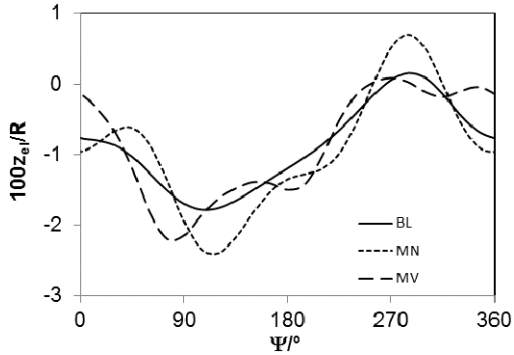

(c) elastic flapping, exp.

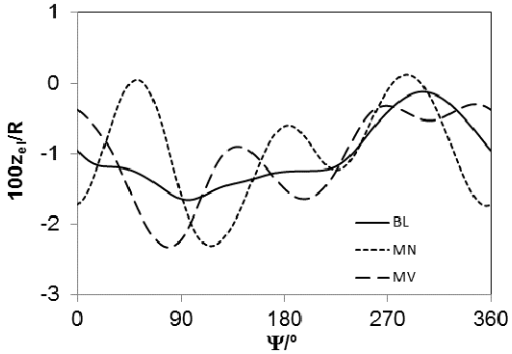

(d) elastic flapping, S4

Figure 8: α_S = +4.5°, 3/rev HHC phase sweep; blade tip motion

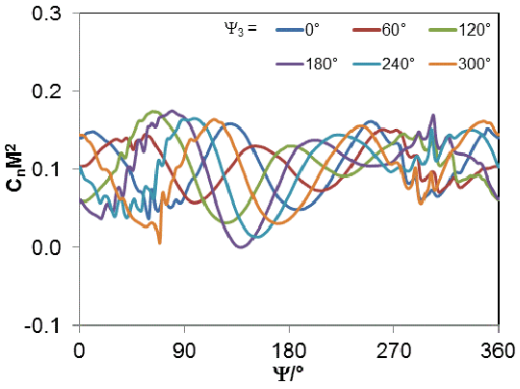

(a) exp.

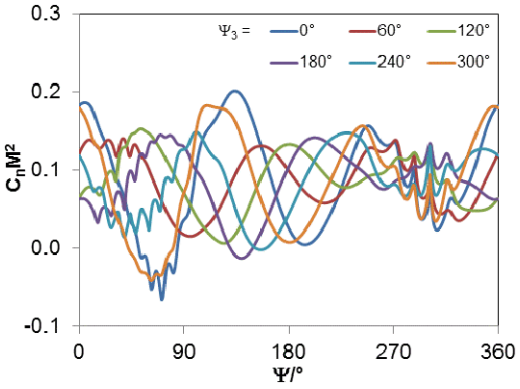

(b) S4

Figure 9: α_S = +4.5°, 3/rev HHC phase sweep; section loading at 0.87R

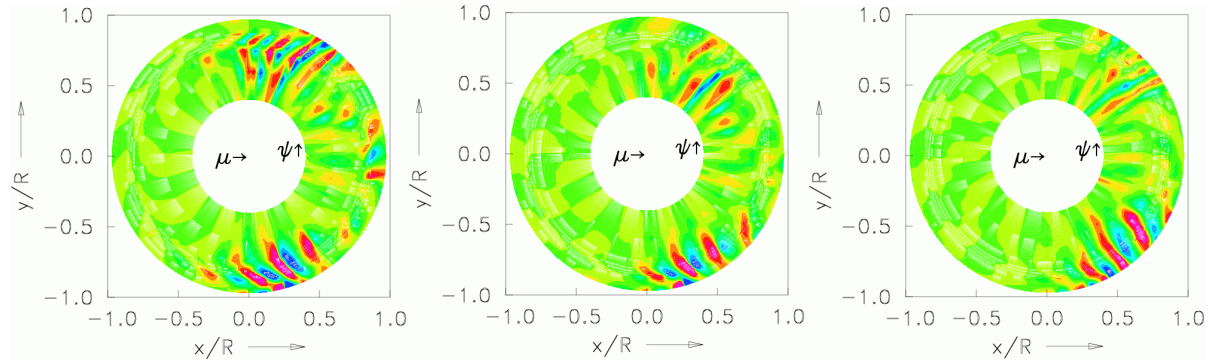

(a) Ψ_3 = 0°, exp. (b) Ψ_3 = 60°, exp. (c) Ψ_3 = 120°, exp.

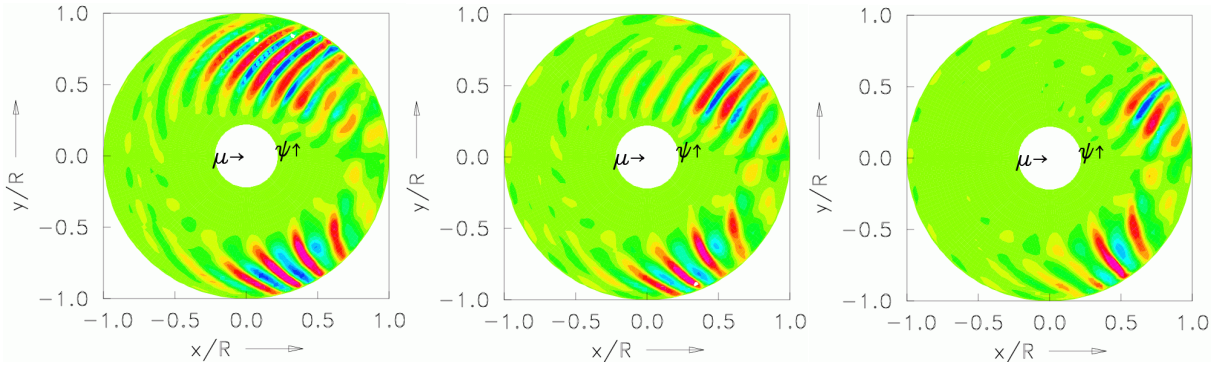

(d) Ψ_3 = 0°, S4 (e) Ψ_3 = 60°, S4 (f) Ψ_3 = 120°, S4

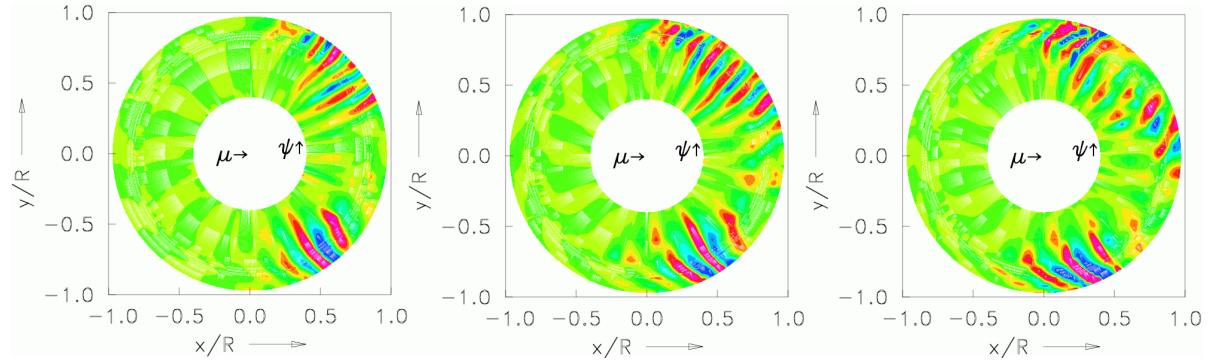

(g) Ψ_3 = 180°, exp. (h) Ψ_3 = 240°, exp. (i) Ψ_3 = 300°, exp.

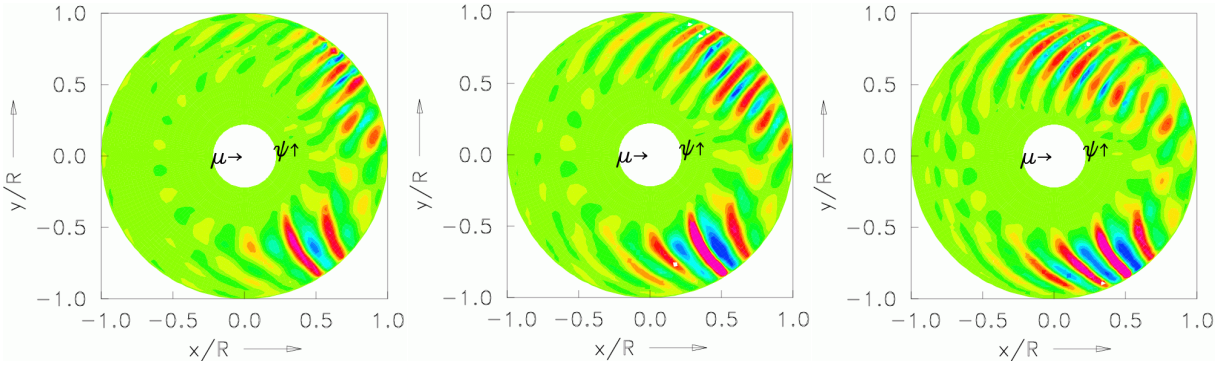

(j) Ψ_3 = 180°, S4 (k) Ψ_3 = 240°, S4 (l) Ψ_3 = 300°, S4

Colors represent 10/rev high-pass filtered contours of $\Delta C_P M^2$ (exp.) and $C_n M^2$ (S4)

Figure 10: α_S = +4.5°, 3/rev HHC phase sweep; BVI locations

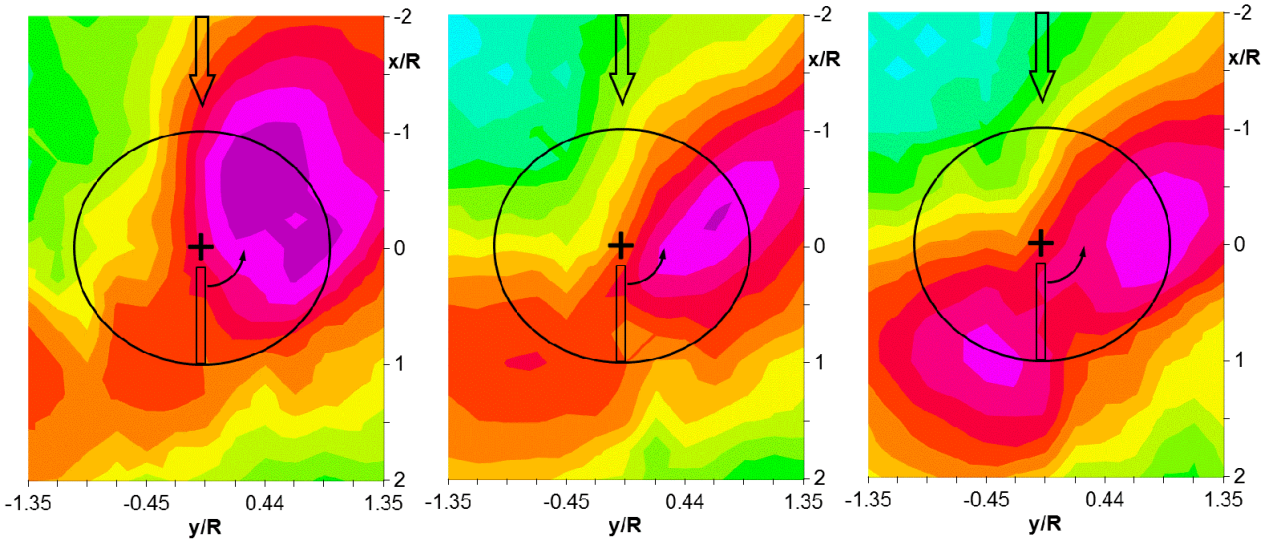

(a) Ψ_3 = 0°, exp. (b) Ψ_3 = 60°, exp. (c) Ψ_3 = 120°, exp.

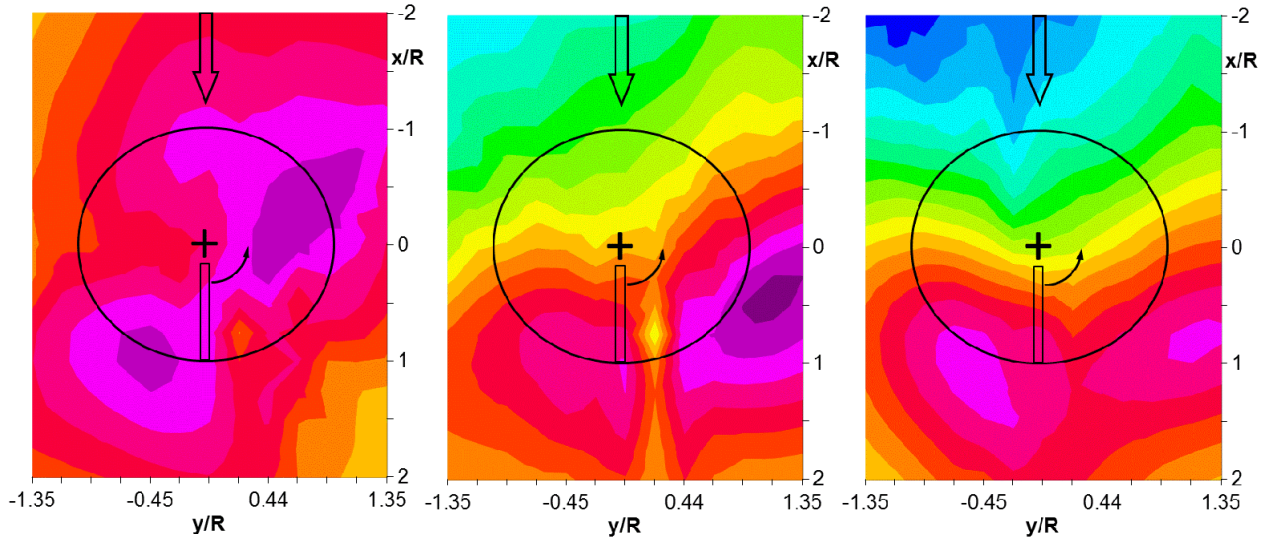

(d) Ψ_3 = 0°, S4 (e) Ψ_3 = 60°, S4 (f) Ψ_3 = 120°, S4

Color scale: mid-frequency noise level (6-40 bpf) from 74 dB (dark blue) to 114 dB (dark violet)

Figure 11: α_S = +4.5°, 3/rev HHC phase sweep; noise radiation (first part)

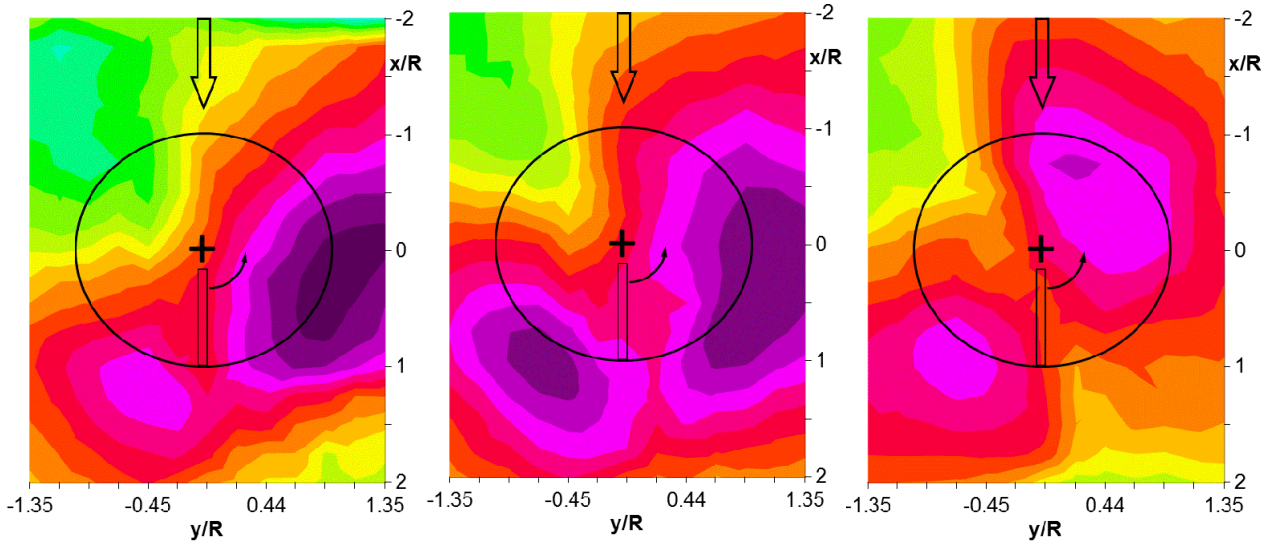

(g) Ψ_3 = 180°, exp. (h) Ψ_3 = 240°, exp. (i) Ψ_3 = 300°, exp.

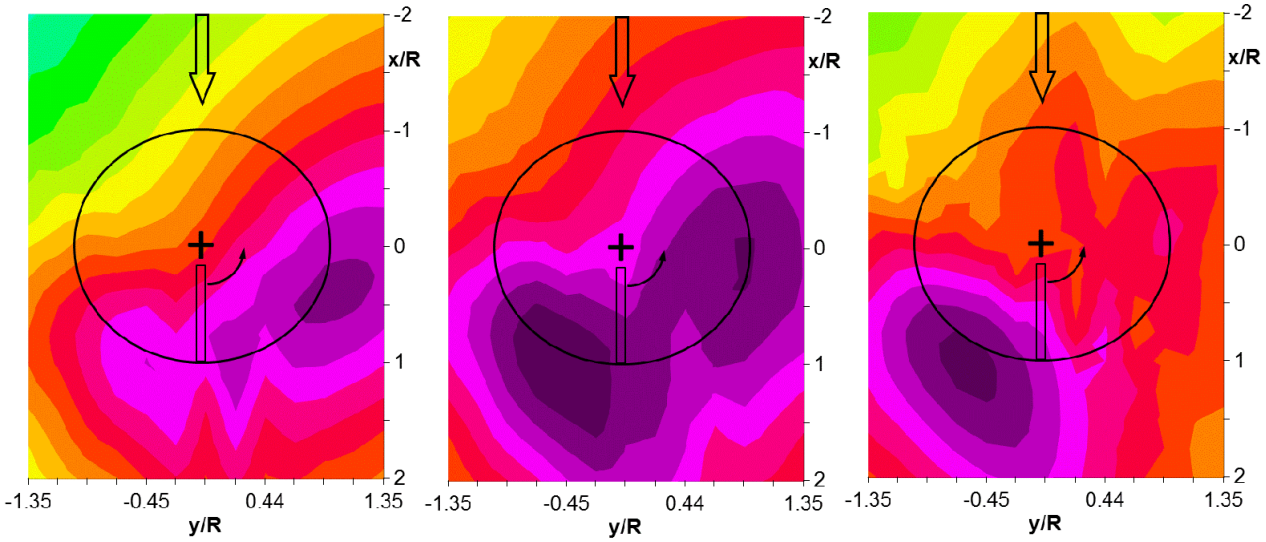

(j) Ψ_3 = 180°, S4 (k) Ψ_3 = 240°, S4 (l) Ψ_3 = 300°, S4

Color scale: mid-frequency noise level (6-40 bpf) from 78 dB (dark blue) to 118 dB (dark violet)

Figure 11: α_s = +4.5°, 3/rev HHC phase sweep; noise radiation (second part)

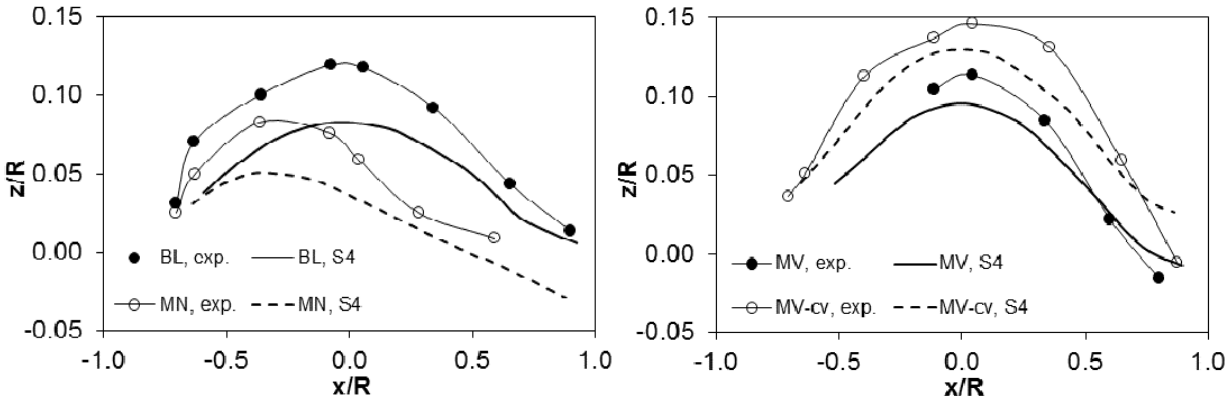

(a) advancing side: BL and MN

(b) advancing side: MV

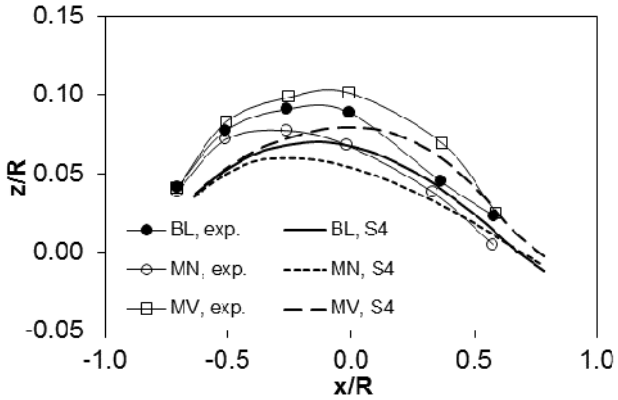

(c) retreating side

Figure 12: α_S = +4.5°; tip vortex trajectories at y = ±0.7R

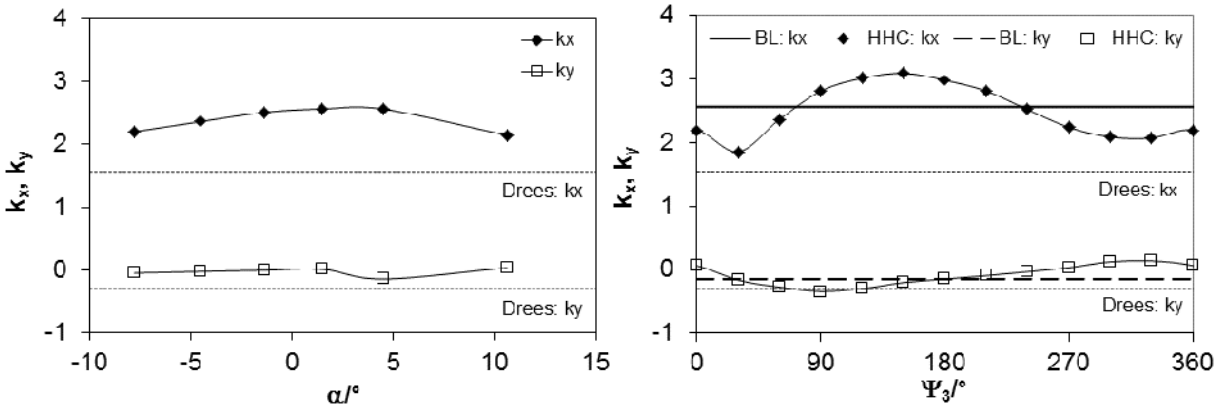

(a) α-sweep

(b) 3/rev HHC phase sweep

Figure 13: α_S = +4.5°; longitudinal and lateral inflow gradients